SAND REPORT

Exploring pulse shaping for Z using graded-density impactors on gas guns

(Final report for LDRD Project 79879)

Michael D. Furnish, Marlin Kipp, William D. Reinhart, Tracy J. Vogler, William W. Anderson and Robert S. Hixson

Sandia National Laboratories

Exploring pulse shaping for Z using graded-density impactors on gas guns

Michael D. Furnish, William D. Reinhart and Tracy J. Vogler
Solid Dynamics and Energetic Materials Department

Marlin E. Kipp
Computational Physics Research and Development Department

Sandia National Laboratories
P.O. Box 5800
Albuquerque NM 87185-1168

William W. Anderson and Robert S. Hixson
Los Alamos National Laboratory
MS P952
Los Alamos NM 87545

Abstract

While isentropic compression experiment (ICE) techniques have proved useful in deducing the high-pressure compressibility of a wide range of materials, they have encountered difficulties where large-volume phase transitions exist. The present study sought to apply graded-density impactor methods for producing isentropic loading to planar impact experiments to selected such problems. Cerium was chosen due to its 20% compression between 0.7 and 1.0 GPa. A model was constructed based on limited earlier dynamic data, and applied to the design of a suite of experiments. A capability for handling this material was installed. Two experiments were executed using shock/reload techniques with available samples, loading initially to near the gamma-alpha transition, then reloading. As well, two graded-density impactor experiments were conducted with alumina. A method for interpreting ICE data was developed and validated; this uses a wavelet construction for the ramp wave and includes corrections for the "diffraction" of wavelets by releases or reloads reflected from the sample/window interface. Alternate methods for constructing graded-density impactors are discussed.

Acknowledgments

We gratefully acknowledge the assistance of Heidi Anderson patiently assembled the projectiles and targets used here. As well, Tom Thornhill and others executed the shots at the STAR facility. Lalit Chhabildas provided a careful review and many helpful suggestions for this report and throughout the project.

Table of Contents

Figures

Tables

Exploring pulse shaping for Z using graded-density impactors on gas guns

1.0 Introduction and Scope

1.1 Introduction

Historically, equations of state have been determined point-by-point via shock loading to Hugoniot conditions. Quasi-isentropic experiments, first on gas guns, and more recently utilizing the smooth magnetic loading of Z and other pulsed-power machines, have made possible measurements of continuous loading curves P(V) for a variety of materials. The basic geometry used on Z is shown in Figure 1.1. Lorentz forces cause loading of the sample plate (anode – on left of current loop shown) with peak stresses from a few GPa to hundreds of GPa. Waveforms are acquired with velocity interferometry as shown. Sample waveforms are shown in Figure 1.2. Generally, analysis has utilized waveforms acquired using two or more samples of different thicknesses, and proceeds by:

(1) Calculating the wave speed C_L at a given free-surface or windowed-surface velocity $C_L = \Delta(\text{thickness})/\Delta(\text{arrival time at same surface velocity})$
(2) Converting the free-surface or windowed-surface velocity to an in-situ velocity U_P
(3) Integrating $dP = \rho_0 * C_L(U_P)*dU_P$
(4) Integrating $dV = - \rho_0 *dU_P / C_L(U_P)$
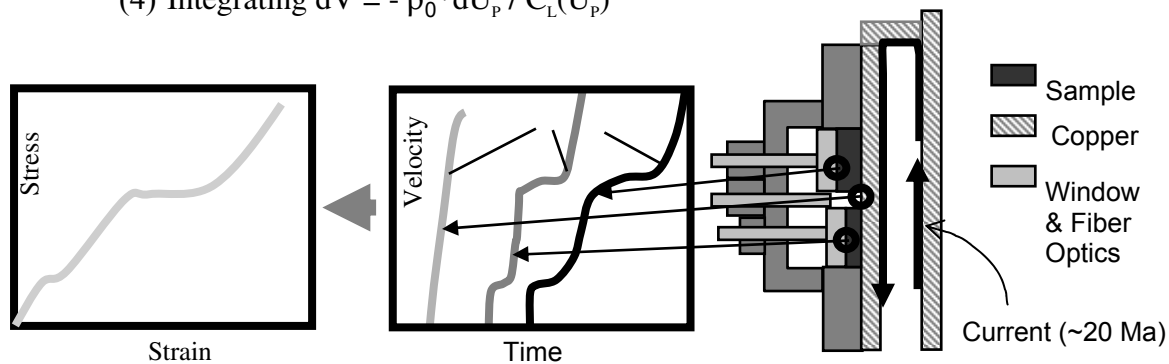
Figure 1.1. Schematic of Z ICE setup (far right), with the measured velocity histories (center) yielding stress strain curve (far left).

The Lagrangian wave speed may be written as $C_L = \text{sqrt}[(\delta P/\delta V)|_s * 1/V_0]$. Hence, if P(V) is strongly concave upward, the wave speed will be a rapidly increasing function of pressure and a ramp will quickly evolve into a shock (the higher-pressure portions of the loading will overtake the lower-pressure portions). This often occurs at low pressures

where pore crushing occurs, or near a large volume-change phase transition (see Fig. 1.2, case of iron $\alpha \rightarrow \varepsilon$ transition). This represents a problem for analysis of ICE because continuous loading information is lost when shock-up occurs. Shock-up also occurs readily in samples loaded to extremely high pressures because of the large disparity between wave speeds at low and high pressure portions of isentropes. For all cases, the use of extremely thin samples may preclude shock-up, but introduces greater imprecision and increased sample preparation difficulties. This difficulty will be even more acute with ZR where isentropic loading to 8Mbar is anticipated.

An alternative approach is to tailor the input loading ramp so that it is gradual in regions of expected large $\delta^2 P/\delta V^2|_s$. This increases the run distance required for shock-up and allows the use of thicker samples. Enabling this approach is the goal of the present proposed effort. Care must be exercised that the samples are not so thin that reflected waves from the surface can reverberate through the sample prior to complete loading.
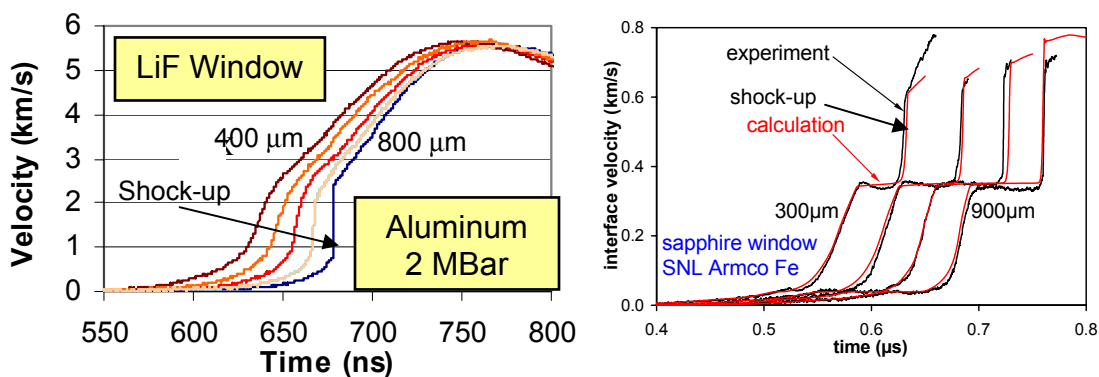
Figure 1.2. Waveforms from ICE loading on Z resulting in ***shock-up*** for aluminum samples (left) to 200 GPa peak pressure and shock up in iron samples to 28 GPa peak pressure. Sample thicknesses are shown.

1.2 Scope

The present study represents a truncated version of a longer study intended to provide and validate a methodology for choosing input loading ramps for use with ICE on Z and other pulsed-power machines for a class of material that undergoes high-pressure phase transformations or large compressions.

We selected a material of interest with an accessible large-volume phase transition, cerium, as a test case. Analyzing the limited available time-resolved experimental dynamic loading data for cerium, we then built an improved material. We obtained samples and executed a portion of a matrix of experiments designed to exercise cerium in nonsimple loading configurations.

As well, to validate the proper functioning of simple graded-density impactors for the simple case of alumina (Al_2O_3), two shots were performed on a compressed gas gun. This represents an updating of earlier ramp-loading experiments in a gas-gun

environment (Chhabildas and Barker, 1986). This differs from pulsed-power ICE primarily in the generation of the compression wave, as shown in Figure 1.3.

To facilitate the interpretation of these and other ICE experiments, we prepared an explicit Lagrangian wavelet analysis code for calculating compression curves from the velocity profiles produced bye two or more samples subject to similar (unknown) ramp loading. This code includes corrections for wavelet refraction due to reloading or release waves returning from the windowed surface.

It may be profitable for future investigators to capitalize on the advent of more advanced sample fabrication and coating techniques driven by needs of the pulsed-power community. With these, it will be possible to construct thinner and more reproducible lamellae. It is also possible to use more materials within a given thickness so as to produce a relatively continuous loading. The progressive increase in pressure with time is provided by stepped increases in the shock impedance of materials within the impactor. Practical materials to use within such an impactor include those shown in Figure 1.4. Utilizing a larger number of layers than in previous studies would allow a smoother loading wave and greater control over waveform (e.g. selection of stress levels for plateaus in the loading wave).

Figure 1.3. Schematic of gas gun graded-density impactor loading, with typical layer thicknesses. VISAR monitors velocity histories at points in target marked by "X" (boundary between samples and windows).

Figure 1.4. Representative materials to use in graded-density impactors.

9

2.0 Cerium: Background and Modeling

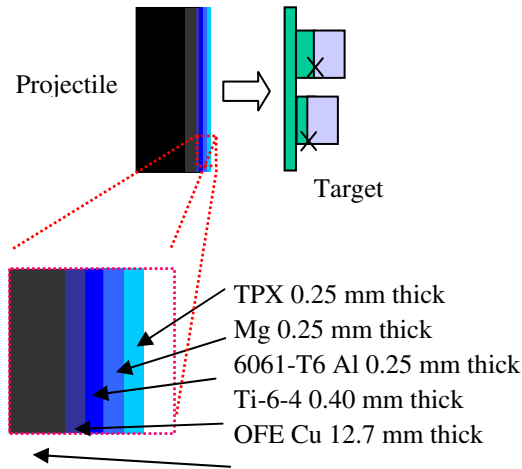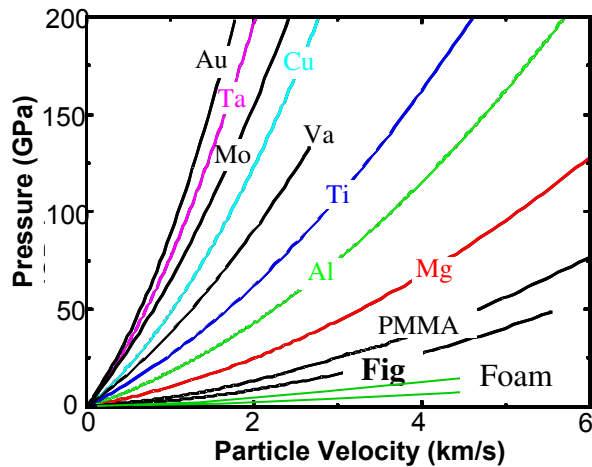## *2.1 Previous Data and Modeling*

Two primary sets of time-resolved dynamic compression data have been reported for cerium: a suite of 5 impact experiments (Anderson, et al., unpublished data, 2003), and a test by Pavlovskii (1999). In addition, several static-compression studies may be found (Singh, 1980; Chesnut, et al., in press; Yelkin, et al., in press). An example of a two phase mixture model to capture the phase transition is included in the Anderson, et al. (2003) summary. As part of that model, the dispersive nature of the low pressure phase, clearly shown in the data of Singh (1980), is represented with a polynomial. Illustration of the model behavior is made by comparing with data for one of the lower pressure experiments; for the case shown, agreement with all aspects of the profile is excellent, including the toe of the wave, the dispersive low pressure wave profile, and the shock to the high pressure phase.

2.2 Material Model Development

The model described in Anderson, et al. (2003) could not be readily implemented into the code to be used for the analyses in the present study, CTH (McGlaun, et al., 1990), but the principles of that approach were used to formulate parameters for a current phase transition model existing within the code – the "PTRAN" model. Within this structure, independent low and high pressure equations of state are used, with the transition defined by its pressure onset, and transitioning from the low pressure phase to the high pressure phase along a prescribed pressure-volume path. Both reversible and irreversible transitions can be accommodated. As in many models, there is tight coupling between all of the constituent aspects of the model, and it was found here that the polynomial reported in Anderson, et al. (2003) needed to be refit for this phase transition model. The only equation of state model in CTH that includes a polynomial representation for pressure vs. strain is the viscoelastic model; this was used for the low pressure equation of state, with a nulling of the viscous behavior, and the polynomial fit to the data of Singh (1990). The high pressure phase was modeled with a linear shock velocity – particle velocity / Mie-Gruneisen equation of state. It was determined that there is a significant discrepancy between the data of Singh and the existing data of Marsh (1980) for cerium. Fits to both data sets were tested against the dynamic compression test velocity profiles.

A summary of much of the data for cerium is shown in Figure 2.1. The anomalous (reverse curvature – dispersive) low pressure region is defined by the Singh (1980) data. For the high pressure phase, the Singh (1980) data have a significantly smaller slope than that of the limited data reported by Marsh (1980). In addition, the Hugoniot points reported by Anderson, et al. (2003) and Pavlovskii (1999) have also been included, and again, there is considerable scatter. The model fit to the data shown here has been adjusted to fit both these data, as well as key velocity profiles from Anderson, et al. (2003):

Low pressure phase – quartic polynomial

$$P(\eta) = k\eta + l\eta^2 + m\eta^3 + n\eta^4,$$ where the volume strain is defined as $\eta = 1 - \rho_0 / \rho$

k=17.6667 GPa, l=-14.58333 GPa, m=-1041.16667 GPa, n=5208.33333 GPa, reference density, ρ_0, of this low pressure phase is 6.774 g/cm^3; onset of the phase transition is prescribed to occur at 0.9 GPa, with a modulus of 5 GPa

High pressure phase – linear shock velocity / particle velocity

Reference density, ρ_0 = 8.30 g/cm^3
Bulk sound speed, c_s = 2.55 km/s
Slope of U_s-u_p curve, s = 0.84
Gruneisen coefficient, γ_0 = 1.0
Specific heat, c_v = 2.1e10 ergs/g/eV

A yield strength of 80 MPa and Poisson ratio of 0.261 were used for deviatoric response.
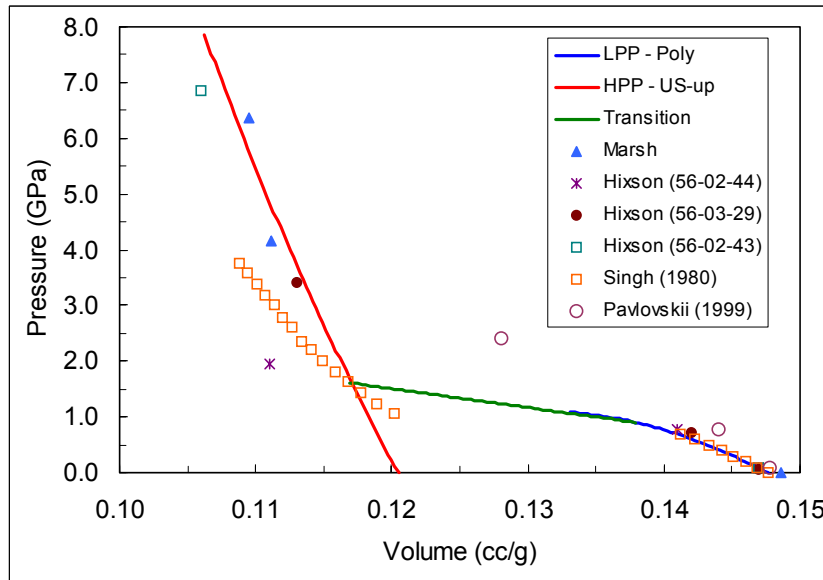
Figure 2.1. Summary of existing cerium data, and model fit.

As noted, these parameters were arrived at after both fitting to the Singh data and adjusting the onset and slope of the phase transition until a good fit was obtained to the Anderson, et al. low pressure wave profile, shown in Figure 2.2. Evident in Figure 2.2 is that using the Singh high pressure data significantly deviates from the wave profile, and that the fit to the Marsh (1980) reported Hugoniot data gives an excellent arrival time and shock to the second phase. In addition, the reported phase transition onset is usually listed as 0.7 GPa (e.g., Singh); the current model requires that to be increased to at least 0.9 GPa in order to match the wave profile data in this figure, and the fit shown in Figure 2.1. Figures 2.3 – 2.6 are the comparisons to the remaining four LANL wave profiles, using the same material model and parameters as for the calculation of the experiment shown in Figure 2.2. In general, the model agreement with the data is quite good.
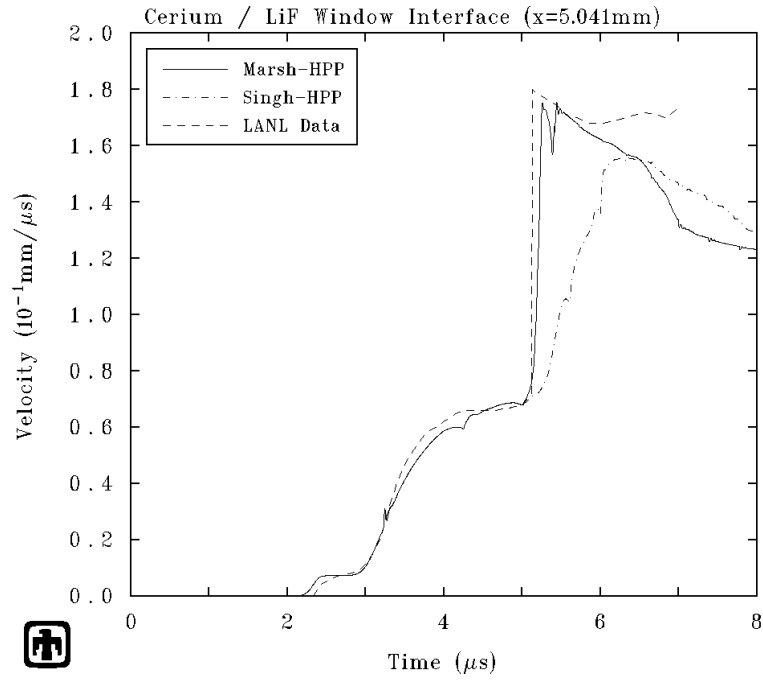
Figure 2.2. Model comparisons to LANL shot 56-02-44.
9.086 mm SS304 (275 m/s) impacting 5.041 mm Ce / LiF window
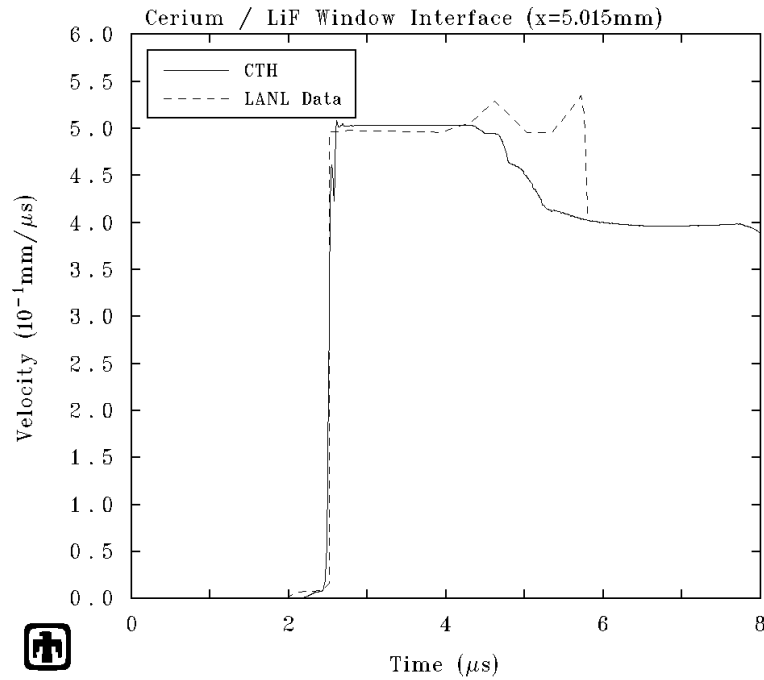
Figure 2.3. Model comparisons to LANL shot 56-02-43.
9.046 mm W (612 m/s) impacting 5.015 mm Ce / LiF window
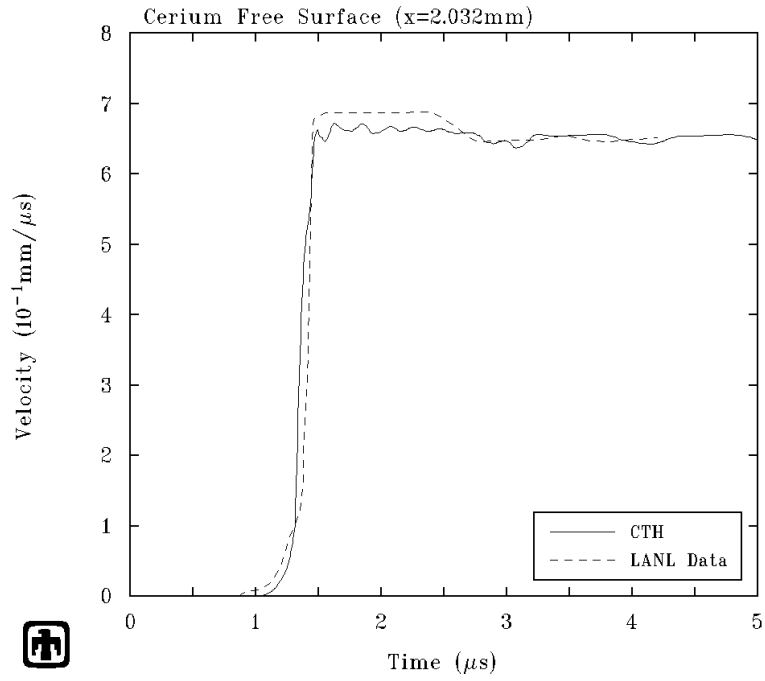
Figure 2.4. Model comparisons to LANL shot 56-03-29.
4.085 mm W (391 m/s) impacting 2.032 mm Ce (free surface)
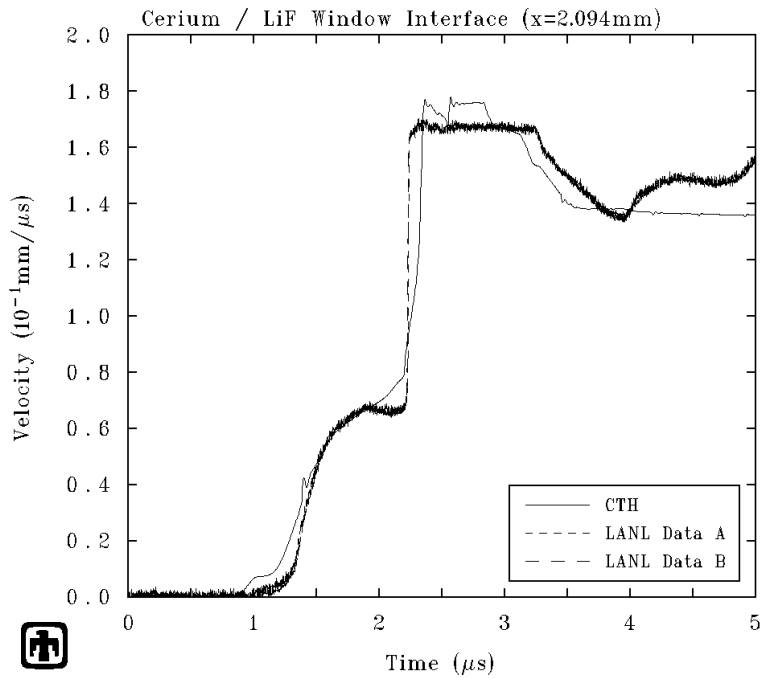
Figure 2.5. Model comparisons to LANL shot 56-04-15.
6.98 mm SS304 (261 m/s) impacting 2.094 mm Ce / LiF window
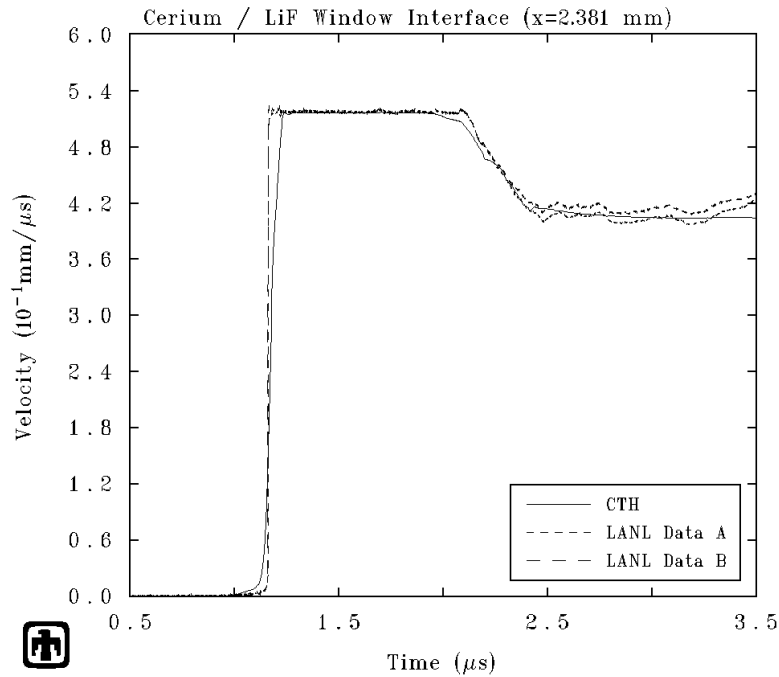
Figure 2.6. Model comparisons to LANL shot 56-04-23.
4.014 mm W (627 m/s) impacting 2.381 mm Ce / LiF window

Using this model, the next application was to try to reproduce the wave profile data reported by Pavlovskii (1999), in which an explosive driver was used to load the cerium. The device geometry was reported as 20 mm TNT / 5 mm gap / 12 mm copper / 9 mm polyethylene / 6 mm copper / 4 mm cerium / 4 mm cerium; the velocity gauge was sandwiched between the two cerium layers to obtain an *in situ* measurement. Timing inconsistencies and failure to obtain satisfactory agreement with those data suggested there might be target thickness and explosive driver geometry uncertainties. One option examined was to place the 5 mm gap in the test configuration between the copper and the polyethylene rather than between the explosive and the copper striker as reported. In either case, as shown in Figure 2.7, using the 4 mm cerium geometry defined in the reported test specifications, timing of the data is quite inconsistent with the model results. The data timing seemed more consistent with a 1.55 mm cerium target plate, and those results are plotted in Figure 2.8. The latter appears to be more representative of the data, but the dispersive leading wave profile transitions to the shock at a lower pressure than the model indicates. The pedigree of the cerium itself may not be exactly as that used in the LANL experiments, to which the model was calibrated, and that would result in some lack of agreement. The major timing difficulties, however, suggest that the reported geometry and data profile are not consistent.

14

Figure 2.7. Model comparisons to Pavlovskii shot; 4mm cerium target.

Figure 2.8. Model comparisons to Pavlovskii shot; 1.5 mm cerium target.

15

3.0 Cerium: Experiments

3.1 Design of Experiment Suite

Recognizing the pivotal role of proper modeling of the $\gamma \rightarrow \alpha$ transition in any low-pressure modeling of cerium, we designed a series of experiments to exercise this transition in various loading configurations. These experiments, designed to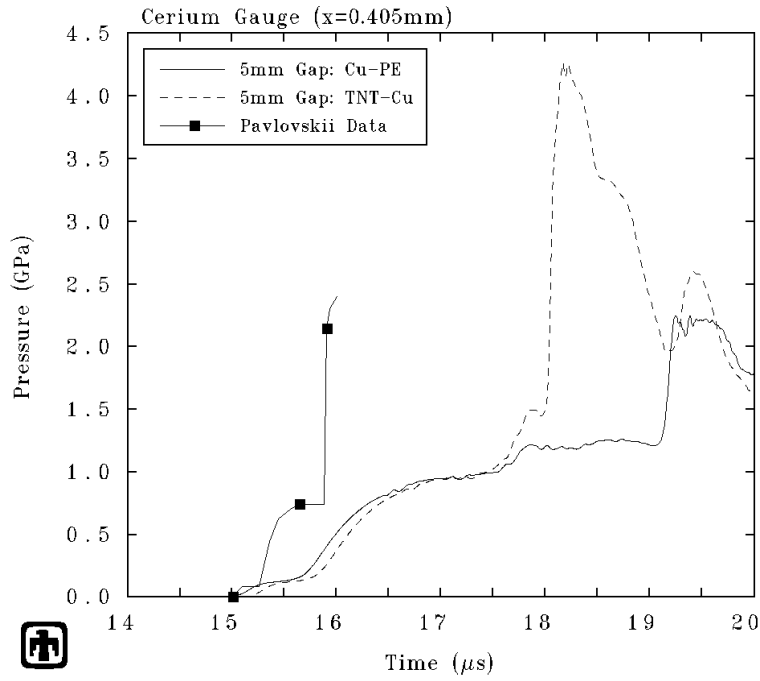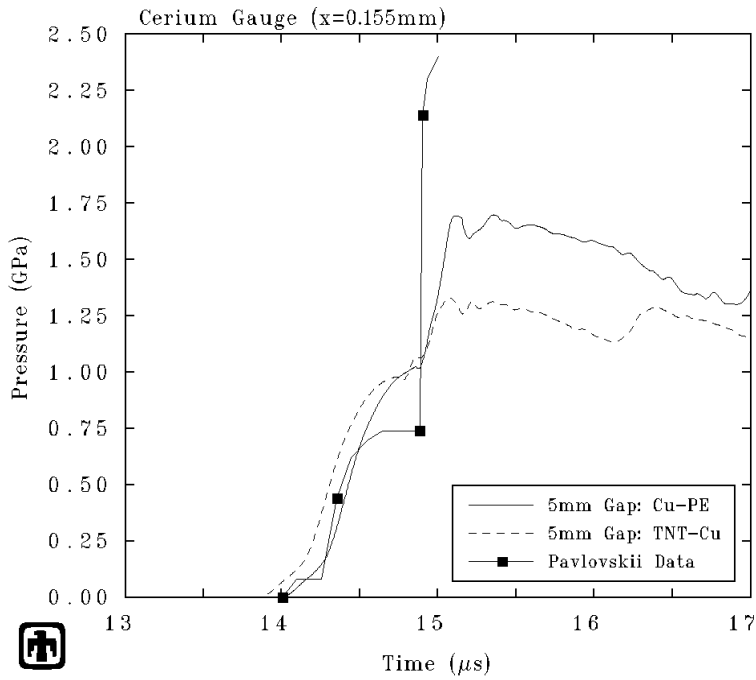 capitalize on capabilities at the STAR facility for multiple simultaneous experiments on each shot, are as follows. For all of these experiments, fused silica windows are used to provide a set of conditions at the measurement point that are close to in-situ.

Set 1: The goal is to assess whether loading to just below the transition, then reloading, causes a different higher-pressure response than loading to just above the transition, then reloading. With a 20% volumetric loss at the $\gamma \rightarrow \alpha$ transition, the effect on the α –phase compressibility may marked, both in terms of energetics and transition kinetics (Fig. 3.1). To this end, a pair of experiments was designed with a 2-layer impactor (PMMA and magnesium) impacting two thicknesses of cerium (backed by fused silica) and a bare fused silica window. Impact velocities of 260 and 300 m/s were chosen to give initial loading to estimated pressures (due to the impact of PMMA onto cerium) of 0.75 and 0.85 GPa. Reloading pressures of 1.3 and 1.55 GPa are expected in the α phase. Pivotal is choosing a PMMA thickness so that the two families of waves are separated, which is difficult because of the large difference between the elastic wave speed and the transition wave speed.
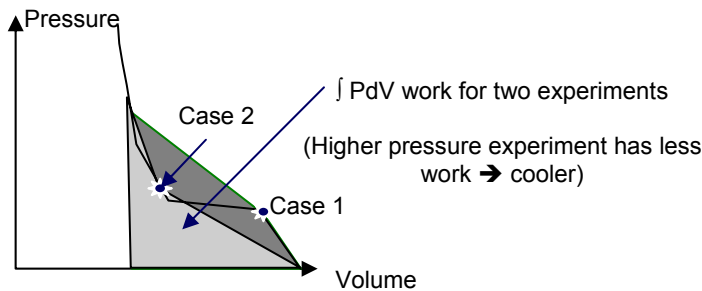
Figure 3.1. Configuration of Set 1. (top left) Schematic of energetics. (bottom left) Timing considerations. (bottom right) Configuration.
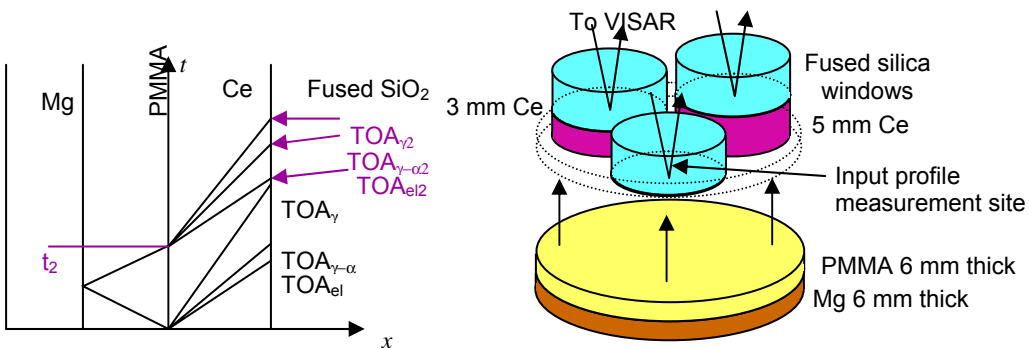
Set 2: The goal is to assess the behavior of cerium using a ramp-wave input produced by a fused-silica buffer impacted by a sharp shock. The ability of fused silica to generate a ramp wave up to approximately 3.5 GPa is well known (Barker and Hollenbach, 1972). Two shots planned (2 samples each) included fused silica impactors impacting 25 mm

fused silica buffers at 222 and 520 m/s. Expected stress levels delivered to the cerium were 1.5 and 3.5 GPa.
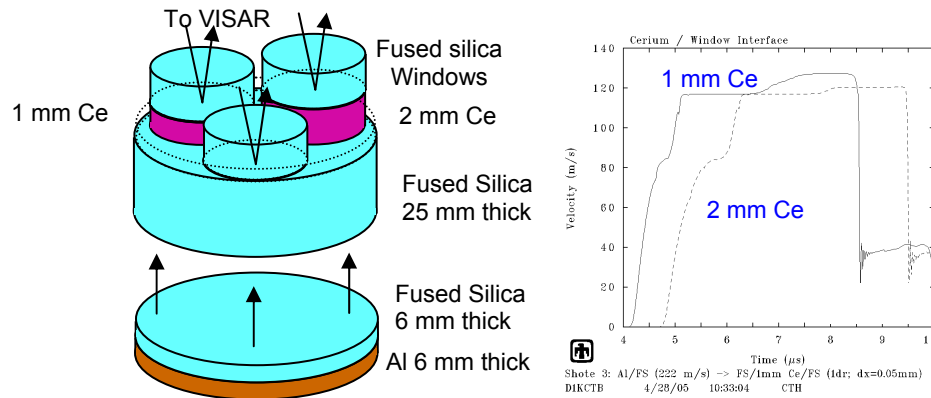
Figure 3.2. (left) Configuration for fused silica ramp-wave input shots; (right) Predicted velocity profiles.

**Set 3:** The goal is to assess the response of cerium on a compressed gun gun to a graded density impactor (GDI) at 328 m/s. A 7-layer impactor (1.000 mm TPX, 0.513 mm PMMA, 0.246 mm Mg, 0.196 mm Al, 0.132 mm Ti, 0.122 mm Cu, > 1.5 mm Ta) impacting at 328 m/s gives an initial loading to 0.6 GPa (slightly short of the $\gamma \rightarrow \alpha$ transition), followed by successive loadings to a final stress of 4.0 GPa.
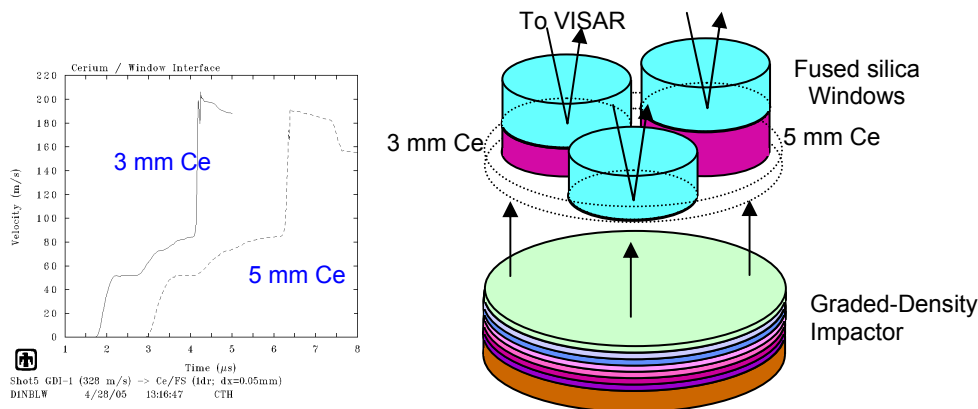
Figure 3.3. (left) Predicted velocity profiles;
(right) Configuration for GDI ramp-wave input shots

**Fused Silica Window Calibration Shot:** The behavior of fused silica as a VISAR window under shock loading has long been established. However, it is not as well known for ramp loading or GDI loading. A shot comprised of a fused silica impactor, a fused silica buffer, fused silica samples as fused windows was designed to elucidate this behavior. Analogous tests have been conducted to characterize the properties of sapphire and lithium fluoride under ramp loading.

17

3.2 Results and modeling

Set 1 was performed, and modeled using the actual parameters of the experiments. Samples were provided by LANL, and are COTS samples from Santuko America. To complete these experiments, a capability for handling the pyrophoric cerium metal was developed at the STAR facility. Experiment parameters are shown in Table 3.1. All fused silica windows were 38 mm in diameter and 25.4 mm thick. Projectile layers (PMMA and magnesium) were 88.8 mm in diameter.

Shot	Ce-1	Ce-2
Impact Vel. (km/s)	0.240*	0.332
PMMA thick (mm)	6.038	6.058
Mg thick (mm)	5.969	5.964
Ce#1 thickness (mm)	2.164	2.187
Ce#2 thickness (mm)	5.100	5.121
Ce#1 density (gm/cc)	6.576	6.572
Ce#2 density (gm/cc)	6.708	6.703
VPF Sensitivities	0.095, 0.138 km/s for both shots	

*Ce-2 impact velocity was 23% lower than planned 0.310 km/s due to burst diaphragm malfunction.

Table 3.1. Shot parameters for shots Ce-1 and Ce-2

The results are shown in Fig. 3.4 (shot Ce-1) and 3.5 (Ce-2). Timing assumed an elastic toe velocity of 2.33 km/s (Anderson et al, 2003). Edge effect issues will be discussed later.

Figure 3.4. Ce-1 results plotted against calculations. Dashed lines are calculations, solid are experiment. Arrows indicate earliest potential edge effects.
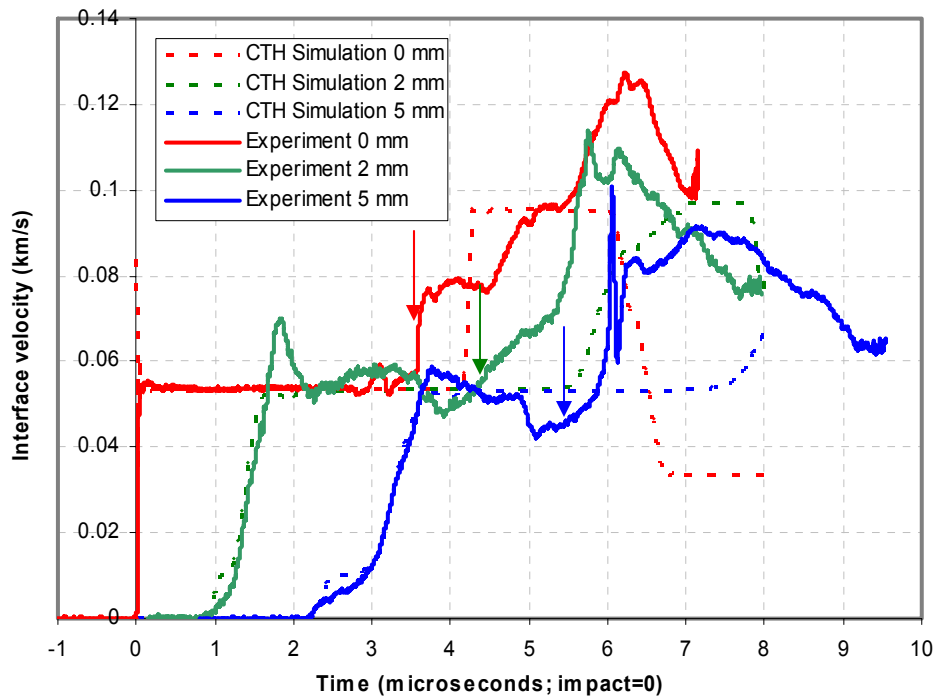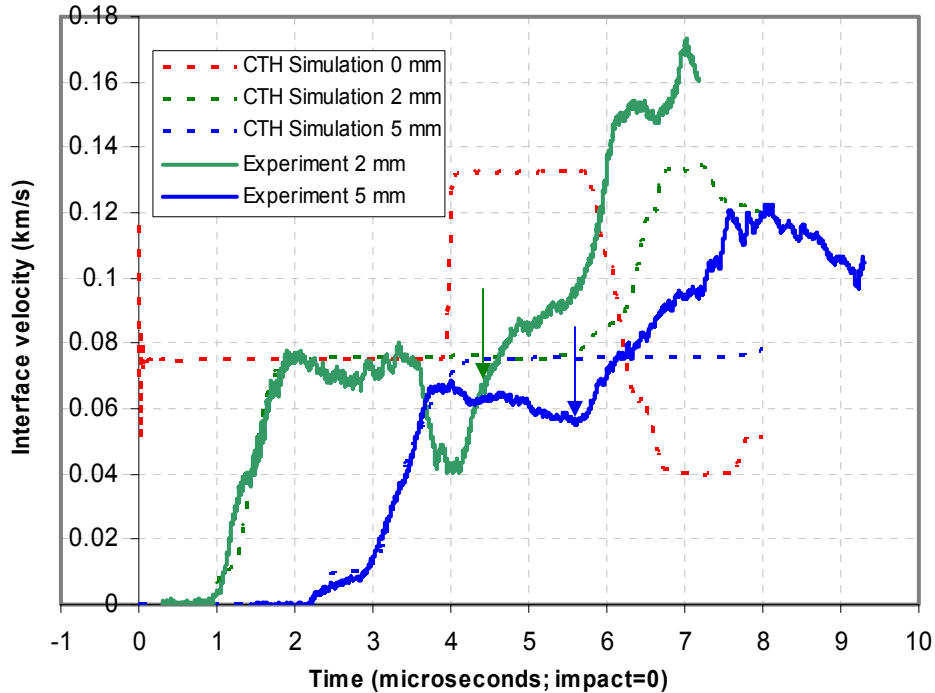
18

Figure 3.5. Ce-2 results plotted against calculations. Dashed lines are calculations, solid are experiment. Arrows indicate earliest potential edge effects.

For both tests, an elastic limit of approximately 1 kb is observed.

In Ce-1, a smooth loading is observed to a stress limited by the PMMA impact stress level (~0.67 GPa), followed by a gradual interface deceleration until the second arrival is observed.(from the reshock generated by the Mg in the impactor). A final loading to roughly 1.1 GPa is observed, with step structures at ~0.8 – 0.85 GPa which may correspond to the onset of a phase transition. These signatures, however, are rather unclear. Had the test fired at its design velocity of 0.32 km/s instead of 0.24 obtained, it is possible a clearer signature of a transition would have been observed.

Test Ce-2 was designed to provide an initial loading to approximately 1 GPa (0.95 GPa obtained). The experimental velocity profiles are observed to fall short of the expected plateau velocity amplitude of 75 m/s, especially for the case of the thicker (5.121 mm) sample. The subsequent loading shows a dispersive wave for both samples at approximately 80 m/s (0.9 – 0.95 GPa).

The Ce-2 data are strongly suggestive of a rate-dependent phase transition, with a marked relaxation shortly before the reshock arrival (2 mm sample) and a lower initial loading (5 mm sample). This is conceivably a cause for the initial peak in shot Ce-1 (2 mm sample); the stress achieved in the initial loading is approximately 0.8 GPa.

The waveforms from both tests were stripped of their reversals for a simple Lagrangian analysis of their compressibility. The "simplified" forms for Ce-1 are shown in Fig. 3.6; those for Ce-2, in 3.7. The Lagrangian analysis used assumes a two-stage loading event, with an intial shock due to a low-impedance impactor and a reshock due to a higher-impedance backer. It does account for the impedance mismatch with the fused

19

silica window. Results of the analysis, shown in Fig. 3.8, show somewhat less
compressibility that expected from the LANL and Singh data (see, e.g., Fig. 2.1).
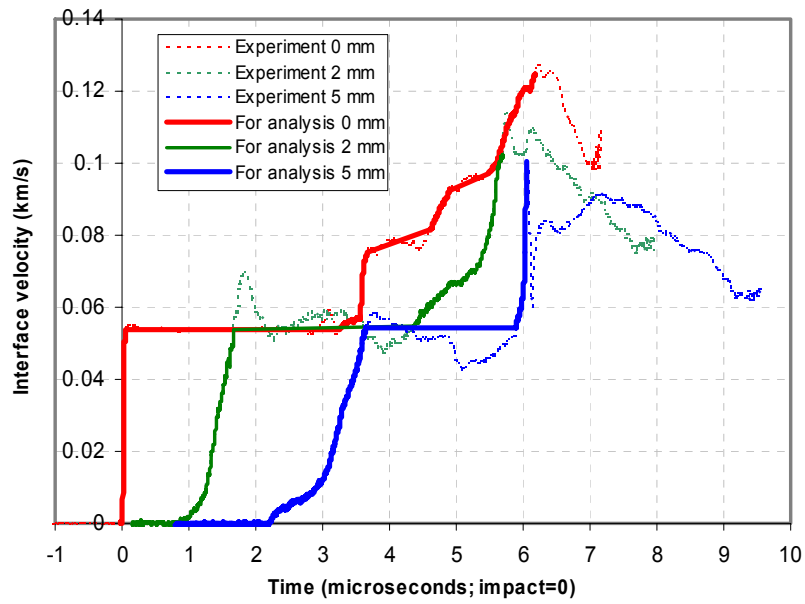

Figure 3.6. Ce-1 results and the simplified waveforms used for Lagrangian analysis.
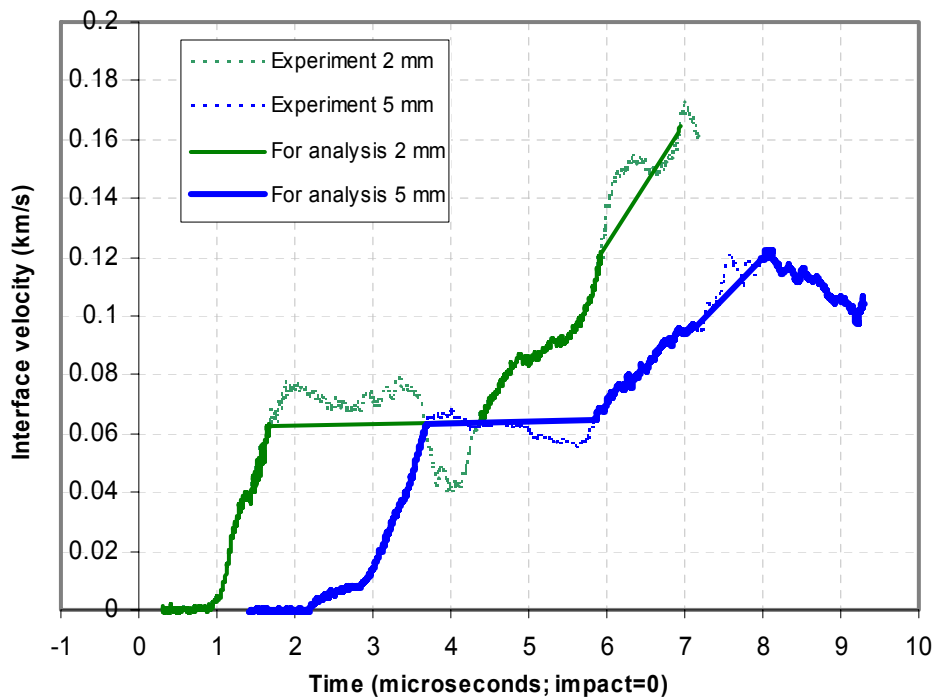

Figure 3.7. Ce-2 results and the simplified waveforms used for Lagrangian analysis.
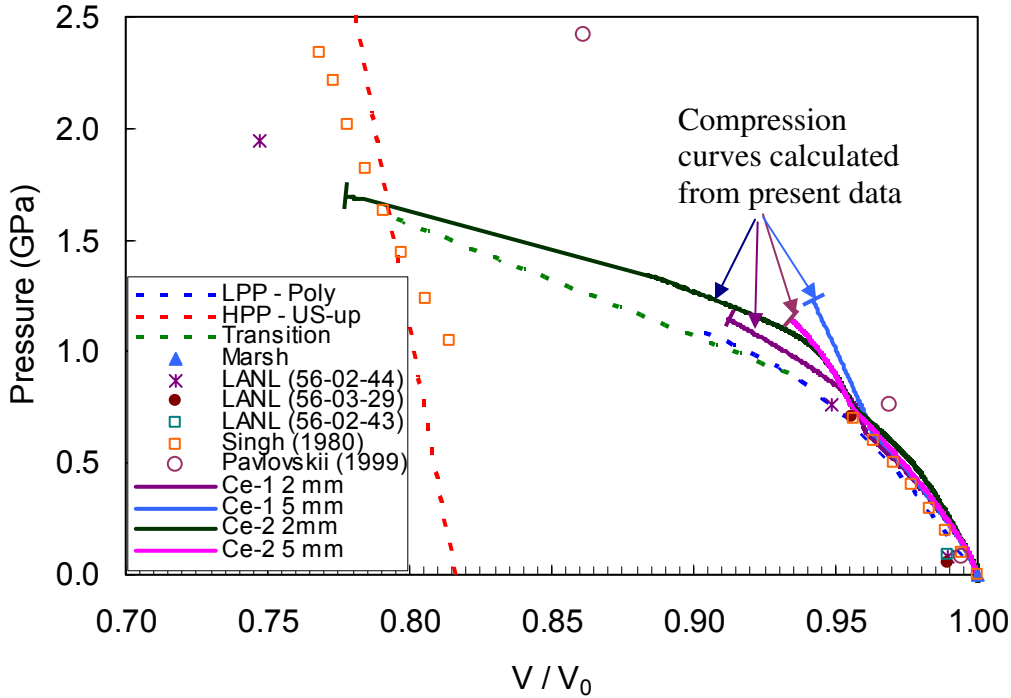
Figure 3.8. Results of Lagrangian analysis for Ce-1 and Ce-2, juxtaposed on model and previous data (cf. Fig. 2.1)

The results indicate that the samples in these experiments are achieving nearly complete transformation of γ to α phase by 1.8 GPa. This is reassuring in light of the fact that the present samples were commercial off-the-shelf. The samples for the Anderson et al (2003) study were specially prepared to be single-phase cerium, but such were not available for the present study. As well, it shows an insensitivity to the difference between the present two-stage loading and the single-wave loading of the LANL experiments.

Edge effects (indicated by arrows in Figures 3.4 and 3.5) represent potential complications to the data. The first such effects are due to waves propagating inward in the fused silica windows at 5.9 km/s (requiring 3.22 μs for the 19 mm radii of these windows). That these were modeled in the CTH runs is reassuring; however, further consideration of the potential effects of edge effects should be made. An earlier design of these experiments had utilized thinner samples to avoid edge effects until later in the experiment; such samples proved unavailable

Further potential experiments of interest abound, including: (1) thinner single-phase samples with a quicker reloading to avoid edge effects, and (2) other ramp-wave experiments as discussed in 3.1. As well, it would be interesting to assess the effects of sample thicknesses on wave profile evolution. In particular, how does the waveform evolve when shocked to 0.7 – 0.9 GPa by a supported wave? As well, the behavior of the mixed-phase region may be better probed via line-imaging VISAR for samples of various thicknesses. This is analogous to heterogeneous strength measurements made with tantalum and other materials (e.g. Furnish *et al*, in press; Chhabildas *et al*, 1990).

21

4.0 Alumina GDI Experiments

With VISAR diagnostics and a modern "pillow" (GDI), we performed two precise ICE experiments with alumina (Coors AD-995). For this material, sapphire windows constitute good windows at least to 14.5 GPa (the yield threshold for Z-cut sapphire). There is evidence (Hayes et al, 2003; also M. Knudson, personal communication) that sapphire retains transparency and reproducible mechanical properties under ICE to much higher pressures than the 14.5 GPa HEL limit observed under single-shock conditions.

The configuration is shown in Fig. 4.1, and the observed waveforms for the first experiment are shown in Fig. 4.2. Timing for these traces was established using the elastic arrivals as fiducials, where the known wavespeed of this alumina is 10.64 km/s.

Layers	mm
TPX	0.587
PMMA	0.513
Mg	0.246
Al	0.196
Ti	0.132
Cu	0.122
Ta	1.519

5.080 mm Al$_2$O$_3$

6.990 mm Al$_2$O$_3$

3.056 mm Al$_2$O$_3$

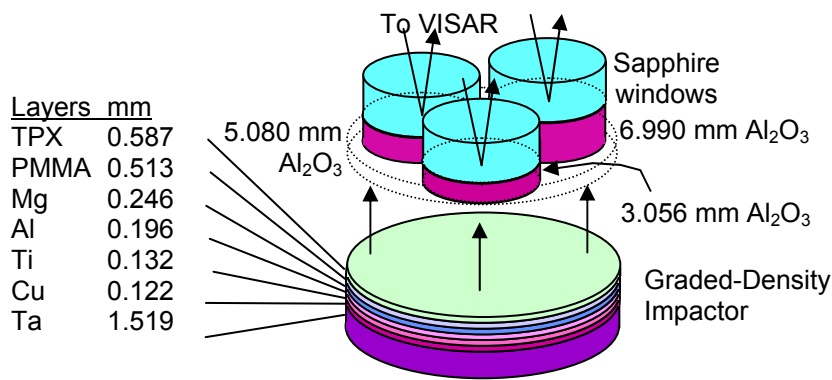Sapphire windows

Graded-Density Impactor

To VISAR

Figure 4.1. Configuration for AD-995 ICE GDI experiments.
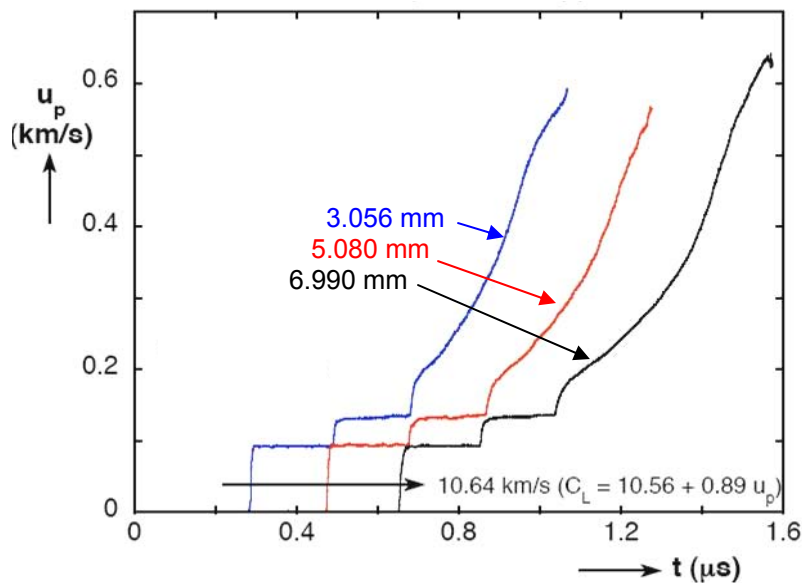

Figure 4.2. Waveforms for the three AD-995 samples on test GDI-1.

The waveforms do show an initial step structure, corresponding to the first three layers

of the impactor (TPX, PMMA and Mg). Later-time sections of the waveforms are much smoother, reflecting the aggregate effect of complicated wave interactions within the individual layers of the impactor.

By methods discussed in Section 6, these waveforms have been analyzed to yield the compression curves shown in Fig. 4.3. These are compared with analogous results from two Z ICE shots (1220 and 1272), which included AD995 alumina samples, and with Hugoniot data from Reinhart and Chhabildas (2003). The exact match to stresses of ~16 GPa is forced by the timing method chosen, while the deviations at higher pressures may be due to a combination of uncertainties in (1) pickoff of the elastic wave arrival, (2) sample variability, (3) sample thickness measurement, and (4) glue bonds.
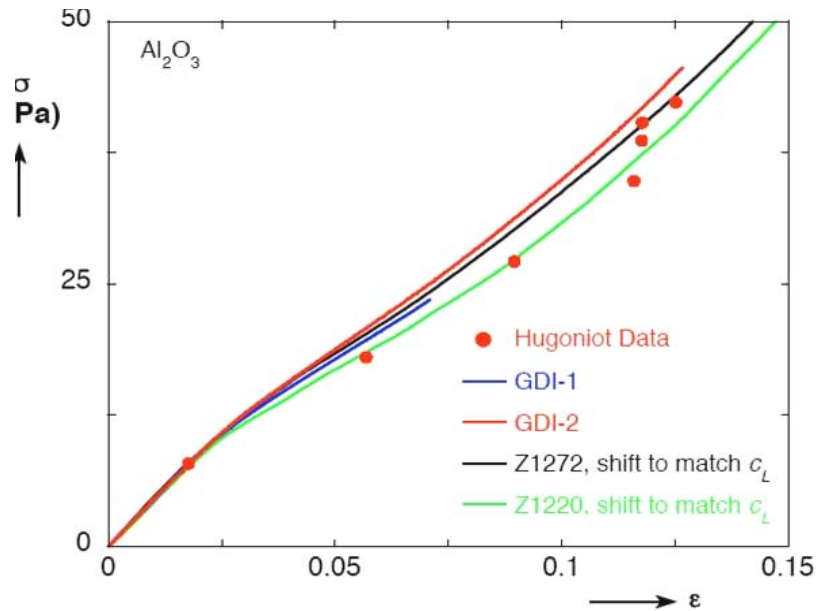

Figure 4.3. Compression curves deduced for AD995 ICE GDI results, compared with Z ICE data and Hugoniot data.

5.0 GDI Fabrication Issues

The properties of graded-density impactors (GDIs) are subject to fabrication constraints. A good GDI may be built in several ways; two of the most practical are (1) a smooth impedance increase from a soft foam to a high-impedance material such as tantalum, and (2) carefully tailored thickness sandwiches to give usable ringup.

For practical sample dimensions, the desired ramp time at the input to the sample is of order 100 ns to 1 microsecond. This is constrained by two factors: (i) Too long a ramp time for a given set of sample thicknesses will allow a complete ringing between the driving interface and the window interface before loading is complete, invalidating the data from the highest part of the loading (Fig. 5.1 left) and (ii) Too short a ramp time will cause shock-up, precluding the derivation of a continuous loading curve from the data (Fig. 5.1 extreme right).
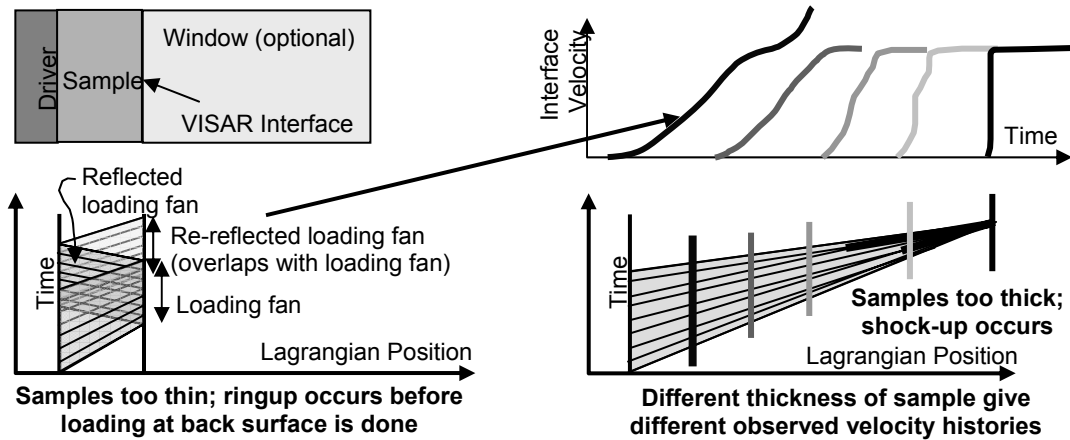

Figure 5.1. Constraints on ramp time used.
Thicker sample and shorter ramp time are equivalent conditions.

For the materials of particular interest in the present study, an objective is to introduce a ramp which does not impose a near-uniform loading rate, but rather, a loading which delays shock-up in the vicinity of a large-volume phase transition (where CL = sqrt$[(dP/dV)|s * 1/V_0]$ changes rapidly with axial stress).

What are typical layer thicknesses? To pursue option (1) above (smooth impedance increase) with a typical 7-layer sandwich, two-way wave transit times in a typical layer must be ~15 – 150 ns; for wave speeds ~4 μm/ns, this means layer thicknesses of 30 – 300 μm. A tailored loading with a pause clearly requires one or more layers to be much thicker. Generally the low-impedance materials need to be thicker to provide a leading "toe" to the ramp because typical sample materials are more compressible at lower pressures; this prevents a shock-up originating at zero pressure.

One avenue to construct GDIs, then, is via plating technologies. The needs of the pulsed-power community have driven advances in these at contractors' facilities supporting SNL (particularly, the Materials Processing and Coatings Laboratory, or MPCL, operated by Ktech). According to J. McKenny (personal communication, 2004), the lowest-impedance materials present particular challenges. Aerogels (density < 0.1

gm/cc) and sol gels can be fabricated in thicknesses up to 10 µm, but the process is labor-intensive. It may be possible to fabricate thicker layers (to 50 microns) using multiple layers, but even this is at the thinnest margin of what may be useful.

For the materials with densities of 0.8 – 1.2 gm/cc, paralyn is easier to deposit than is PMMA, which would require a spin-coat. However, thicknesses greater than 5 µm are difficult, although McKenney (2004) considers 100 µm to be possible. Core drilling such sheets, though, would be difficult.

At greater densities, metals may be plated to thicknesses of roughly 100 µm. Tin, aluminum, copper and gold are good candidates. Lower-Z metals such as B, Mg and Be are more difficult to plate, as are MgF and MgO. CVD deposition at the required thicknesses is probably not plausible.

A second avenue for constructing GDIs is via material lamination (carefully gluing selected foils together). Because of the much smaller lead-time of this approach, we began with this (see Section 4).   Material thicknesses are generally dictated by commercially available foils with this approach unless a substantial manufacturing resource is available.

Other methods for fabricating GDIs (e.g. sedimentation) are beyond the scope of the present project.

6.0 Lagrangian Analysis

This section discusses an explicit Lagrangian ICE wavelet analysis program, ICE1, developed to allow the rapid calculation of stress-strain paths from ICE experiments. Currently this program is operational for some cases, but requires further work for other cases.

6.1 Purpose

In an ICE experiment (this is actually redundant - ICE means Isentropic Compression Experiment), a ramp loading is introduced into two thicknesses of samples, and waveforms are measured at the distal surfaces of the samples. The goal is to determine a continuous curve representing the pressure-volume (compressibility) behavior of the sample material to whatever stress amplitude is introduced into the sample.

The only information assumed to be in hand (in an instruction file) is:
- The $2 - 8$ velocity histories, with accurate relative timing,
- Initial density of the sample material, and
- What the window material is (the analysis program should contain information about the required properties of this material).

In addition, the operator specifies in the instruction file:
- Size of each step of velocity (wavelet) to be used
- Time interval of interest for each velocity history

6.2 Operation

ICE1 begins by representing each velocity history as a series of wavelets (small steps in velocity at the window). Typically $30 - 200$ are used to span the velocity change observed in the wavefront. Grady and Young (1976) mention 30 as a workable number, but it is an easily adjustable parameter. ICE1 includes an algorithm for making a reasonable guess as to what time assignment to apply to a step in a noisy waveform, and can be instructed to produce a data file containing the step structure which may be plotted over the original data for verification purposes.

At present, this program does not support calculating release paths. This is a possible future addition, analogous to the older characteristics code IMP (Grady and Young, 1974).

Let us consider the wave interactions with windows or free surfaces. It is this portion that is new to ICE1. If we take the compression wave passing through the sample as a set of wavelets (small steps), its behavior when encountering a window (or an interface with any other material) may be represented as shown in Figure 6.1.

Here, the successive states 1, 2, 3 ...may all be characterized by axial stress, material velocity (particle velocity), wavelet speed, and sample density (or alternatively specific volume or strain). Other quantities such as specific energy may be derived later if desired. The relations between axial stress and particle velocity are enforced by the Rankine- Hugoniot equations and continuity requirements, graphically represented as stress-particle velocity plots (for details, see McQueen et al (1970)).
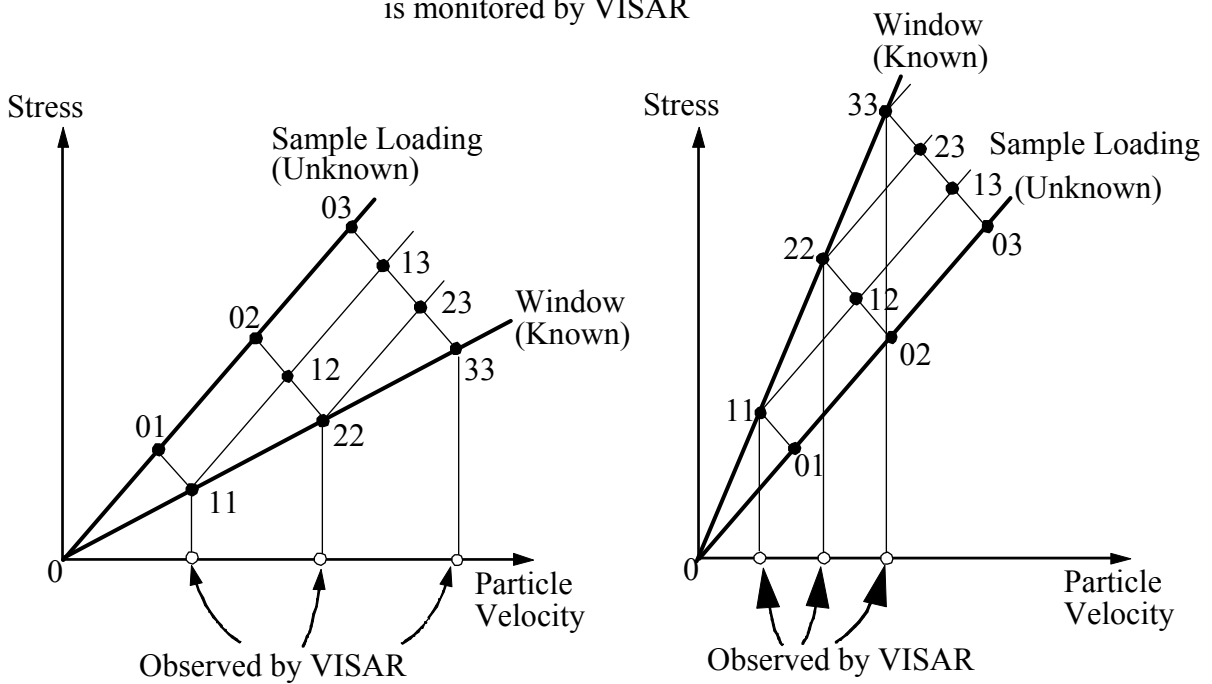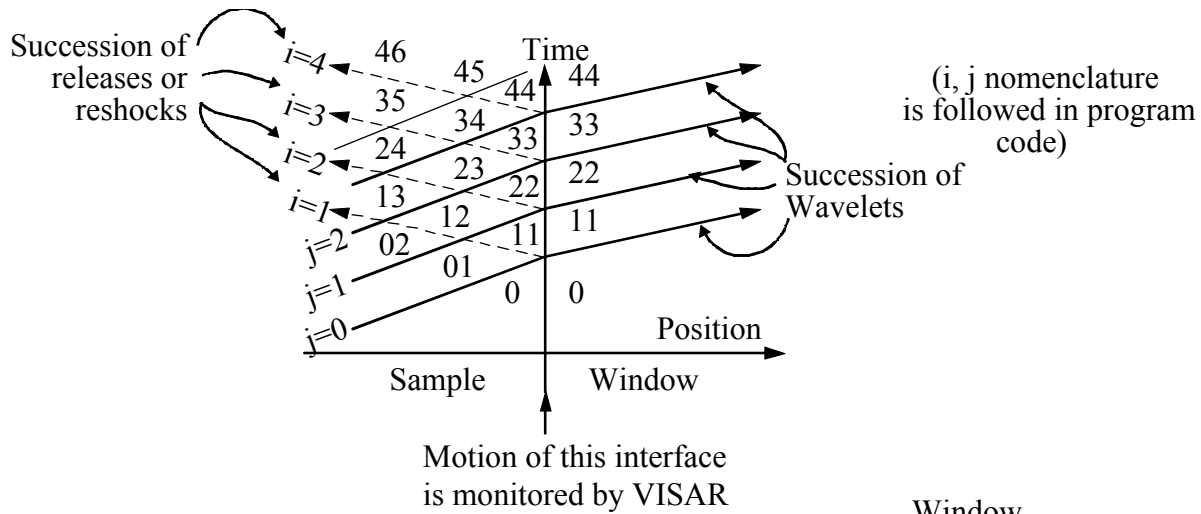
Figure 6.1 Wave interactions with windows. (Top) x-t diagram. (Left bottom) P-Up diagram, window has lower impedance than sample. (Right bottom) P-Up diagram, window has higher impedance than sample. Some problems combine both cases. Releases and reshocks (e.g. line from 02 to 22) may be considered to have the same slope as sample load path (line from 0 to 03).

The case where the window is replaced by a free surface is shown in Figure 6.2.

The compression curve is determined via information about the wavespeed through the sample. For a given wavelet, this is:

$$C_L = T_{12}/(t_2 - t_1) \qquad\qquad \text{(Eq. 1)}$$

where T_{12} is the difference in sample thicknesses, and t_1 and t_2 are the arrival time of the given wavelet for samples 1 and 2, respectively. "Lagrangian" means referenced to the original (uncompressed) dimensions of the sample.

Take P to mean axial or longitudinal stress. The local slope of the stress/volume curve is given by Eq. 2 (at wavelet conditions). Here we are writing P where strictly the
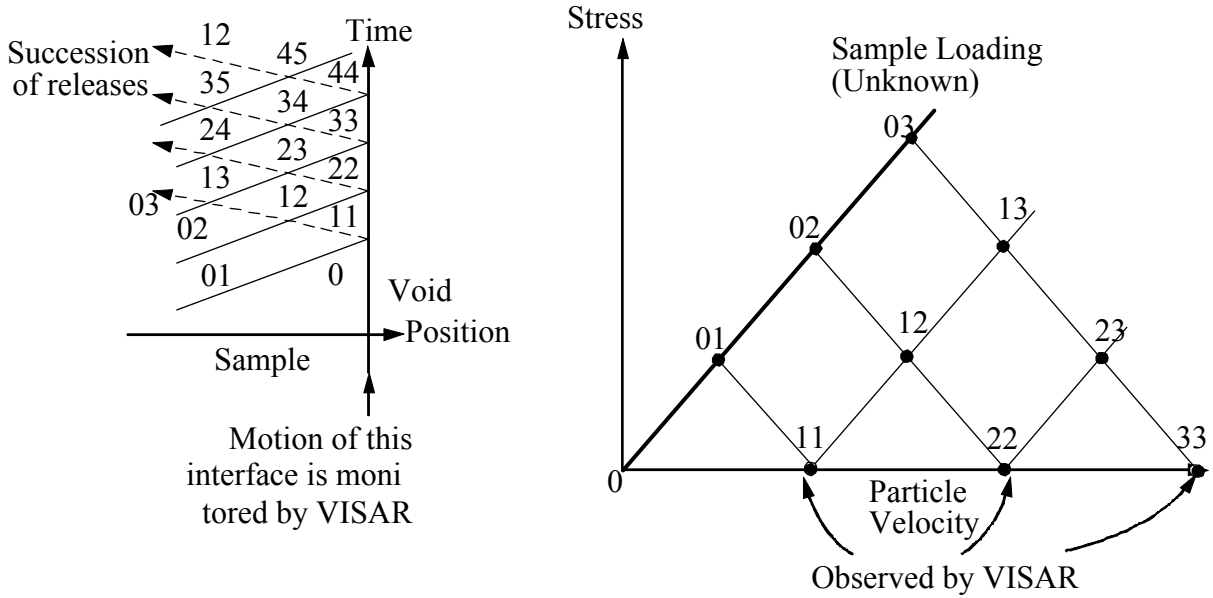
Figure 6.2 Wave interactions with free surface. (Left) x-t diagram. (Right) P-Up diagram. *Releases and reshocks (e.g. line from 12 to 13) have essentially the same slope as sample load path (line from 0 to 03).*

longitudinal stress, σ_{long}, is meant.

$$C_L = \frac{V}{V_0}C_E = \sqrt{\left.\frac{\partial P}{\partial(V/V_0)}\right|_S} \quad \Rightarrow \quad \left.\frac{\partial P}{\partial V}\right|_S = C_L^2 V_0 \qquad \text{(Eq. 2)}$$

The wavelets are measured in terms of particle velocity at the sample/window interface (or sample free surface). So the stress condition of the sample must be calculated. The method for doing so is shown graphically in Figures 6.1 and 6.2 (the stress/particle velocity plots). Actually quantifying these results requires converting the sample stress-volume curve to a stress-particle velocity curve. For a single shock wave, the Rankine-Hugoniot equations give Eq. 3:

$$U_P = \sqrt{(P - P_0)/(V_0 - V)} \qquad \text{(Eq. 3)}$$

Hence the increase in particle velocity with the passage of a weak shock may be written:

$$\Delta U_P \equiv U_{P,\,i+1} - U_{P,\,i} = \sqrt{(P_{i+1} - P_i)(V_i - V_{i+1})} = \sqrt{-(\Delta P \Delta V)|_S} \qquad \text{(Eq. 4)}$$

The slope of the sample loading curve in stress - particle velocity space for isentropic loading may be written as:

$$\frac{\partial P}{\partial U_P}\bigg|_S = \left(-\frac{\partial P}{\partial V}\bigg|_S\right)^{\frac{1}{2}} \qquad \text{(Eq. 5)}$$

From Eqs. 2, 5 and 6, then, we are able to calculate the sample paths in stress vs. particle velocity space. This in turn allows the calculation of the sample state (A, B, C, ...) by the method shown graphically in the bottom plots of Figures 2 and 3' this is the goal of the program. In other words, the calculation uses results to date to calculate the stress, particle velocity and specific volume for each new state (next wavelet).

In practice, the solution is iterative. A stress-strain curve for the sample is calculated as above. Next the "refraction" of the wavelets due to interaction with the backward-moving wavelet reflections from the window or free surface is calculated. This is a complicated accounting process which requires calculating the sample state in each wavelet interaction zone (ij) (Figs. 6.1 and 6.2). For experiments with windows of higher impedance than the sample, the procedure is further complicated in that the first iteration requires guessing the reshock properties of the sample, and correcting in subsequent iterations. Finally, knowing the refraction effect on the arrival time of the wavelets at the interface, it is possible to correct the transit time for this effect.

Attenuating waves (Fig. 6.3) create a "least-common-denominator" situation in which the properties of the sample material may only be extracted to the pressure of the most-attenuated waveform observed. In addition, the program does not currently correctly calculate compression curves for waveforms where major dips occur in the wavefront.
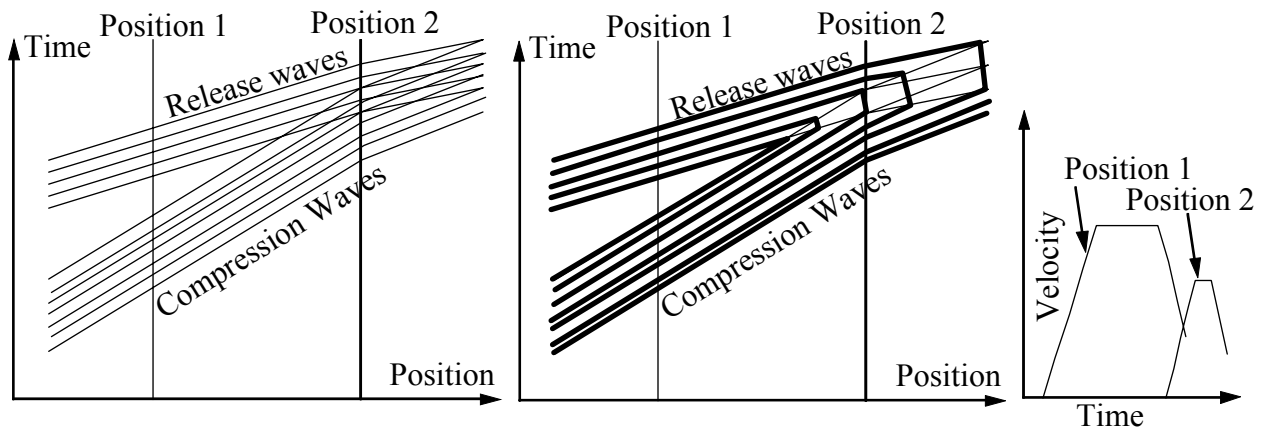

Figure 6.3   Example of attenuating wave. (Left) Wavelets. (Center) Characteristics (velocity or stress contours) (Right) Measured velocity histories.

6.3 Results of trials

An initial trial was conducted with Z524, an experiment including molybdenum samples and LiF windows. This provided a good test case including a large impedance mismatch between the samples and the windows. Wave profiles are shown in Fig. 6.4.
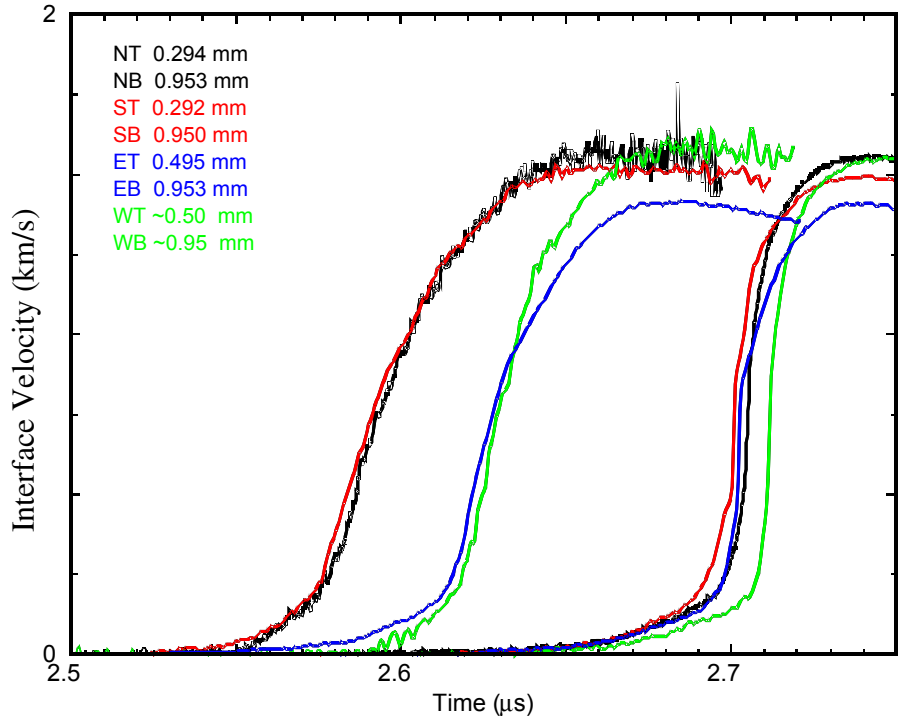
Figure 6.4. Velocity profiles from Z524 (Mo samples, LiF windows)

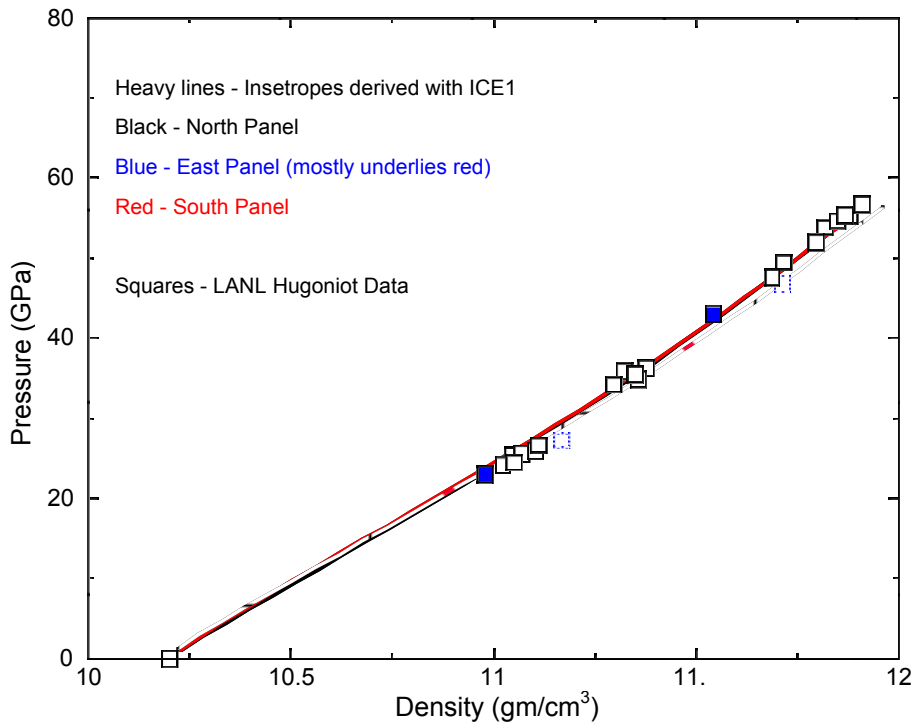The deduced compression curve here is substantially in agreement with earlier Hugoniot data (Fig. 6.5).

Figure 6.5. Deduced Mo isentrope from Z524

A second trial with data from Z1081 (samples 1 and 4 on the north panel) was conducted to exercise higher-pressure issues, involving aluminum samples (0.760 and 1.561 mm thick) loaded to > 150 GPa. Two models of the LiF windows were assumed: an isentropic loading construct provided by J-P. Davis and a Hugoniot representation. Results for the deduced wave speeds are shown in Fig. 6.6. The isentropic window representation produces lower aluminum particle velocities for a given wavelet speed than does the Hugoniot LiF representation because the isentropic representation is softer. The corresponding aluminum compression curves are shown in Fig. 6.7.
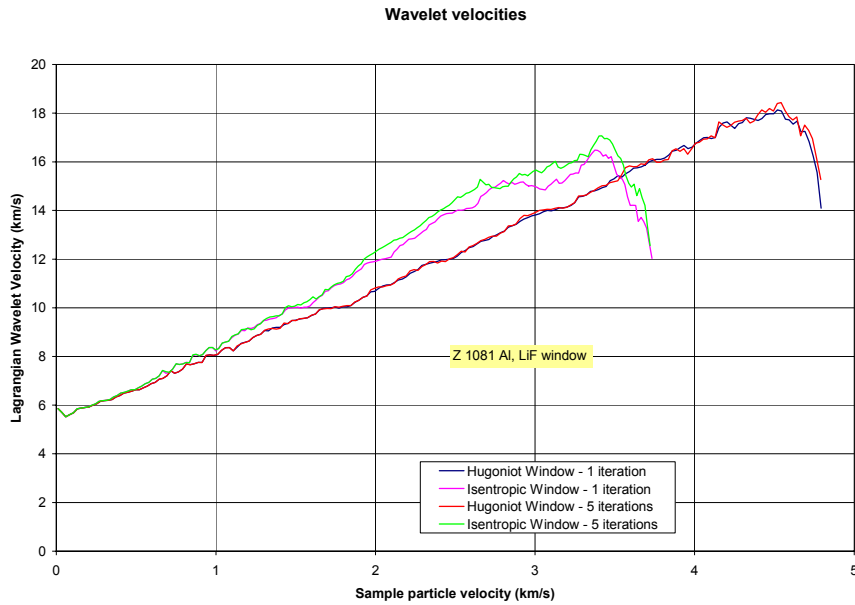
Wavelet velocities

Figure 6.6. Z1081 aluminum sample wavespeeds for two window models (ICE1)
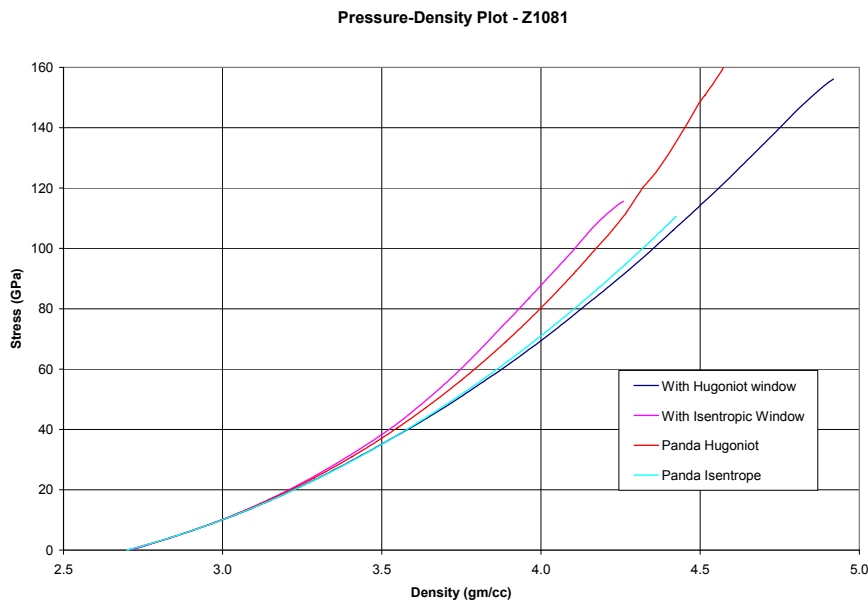
Pressure-Density Plot - Z1081

Figure 6.7. Aluminum pressure-density plots deduced from ICE1 (Z1081), compared with PANDA models for the Hugoniot and isentrope.

A third, low pressure, trial is described in Section 4 for the case of alumina loaded with GDIs to 22 and 45 GPa.

This analysis method does not account for rate dependence. On the other hand, it is model independent (for the sample). This allows the extraction of loading yield data as well as calculating volumetric change information for multiple transition events. As well, it does not require a knowledge of the input wave structure.

References

Anderson, W. W., D. B. Hayes, R. S. Hixson and G. N. Chesnut, Phase transformations and dynamic compression of cerium, presentation at 2003 APS Topical Conference on Shock Compression of Condensed Matter, Portland OR.

Barker, L. M. and R. E. Hollenbach, Shock wave studies of PMMA, fused silica and sapphire, J. Appl. Phys., 41, 4208-4226, 1970.

Chhabildas, L. C. and L. M. Barker, Dynamic quasi-isentropic compression techniques: Applications to aluminum and tungsten. Sandia National Laboratories report, SAND86-1888, 1986.

Chhabildas, L.C., W. M. Trott, W. D. Reinhart, J. R. Cogar and G. A. Mann, Incipient spall studies in tantalum – microstructural effects, pp. 483-486 in Shock Compression of Condensed Matter – 2001, M. D. Furnish, N. N. Thadhani and Y. Horie (eds), AIP Press, 2002.

Furnish, M. D., W. D. Reinhart, W. M. Trott, L. C. Chhabildas and T. J. Vogler, Variability in dynamic properties of tantalum: Spall, Hugoniot elastic limit and attenuation, Shock Compression of Condensed Matter – 2005, M. D. Furnish, M. E. Elert, T. P. Russell and C. T. White (eds), AIP Press, in press (est).

Grady, D. E. and E. G. Young, Evaluation of constitutive properties from velocity interferometer data, Sandia National Laboratories Report SAND 75-0650, 1976.

Hayes, D. B., Hall, C. A., Asay, J. R., and Knudson, M. D. (2003), "Continuous index of refraction measurements to 20 GPa in Z-cut sapphire," J. Appl. Phys. 94, 2331-2336.

Marsh, S. P. (1980). "LASL Shock Hugoniot Data," University of California Press, Berkeley.

McGlaun, J. M., S. L. Thompson, and M. G. Elrick (1990). "CTH: A Three-Dimensional Shock Wave Physics Code," Int. J. Impact Engng., Vol. 10, pp 281-294.

McQueen, R. G.,, S. P. Marsh, J. W. Taylor, J. N. Fritz and W. J. Carter, The equation of state of solids from shock wave studies, pp. 293 - 417 in *High Velocity Impact Phenomena*, R. Kinslow (ed.), Academic Press, 1970.

Pavlovskii, M. N., V. V. Komissarov, and A. R. Kutsar (1999). Isomorphic $\gamma \rightarrow \alpha$ Phase Transition of Cerium under Shock Compression," Combustion, Explosion, and Shock Waves, Vol. 35, No. 1, pp 88-91, 1999.

Reinhart, W. D., and Chhabildas, L. C. (2003). "Strength properties of Coors AD995 alumina in the shocked state," Int. J. Impact Eng. 29, 601-619.

Singh, A. K. (1980). Volume compression of cerium up to 4 GPa," High Temperatures – High Pressures, Vol. 12, pp 47-59, 1980.

Yelkin, V. M., E. A. Kozlov, E. V. Kakshina, Yu. S. Moreva (2005). "Two-Phase (γ,α) Equation of State for Cerium and Features of its Dynamic Compression," submitted for publication in Shock Compression of Condensed Matter – 2005, M. D. Furnish, M. E. Elert, C. T. White and T. P. Russell, eds, AIP Press, in press.

Distribution